Acta Materialia 286 (2025) 120727

Contents lists available at ScienceDirect

Acta Materialia

journal homepage: www.elsevier.com/locate/actamat

Full length article

Nonlinear elasticity degrades monolayer fracture toughness

Israel Greenfeld [a,*,1], Shenda Jiang [b,1], Lin Yang [b,*], H. Daniel Wagner [a,*]

[a] Department of Molecular Chemistry and Materials Science, Weizmann Institute of Science, Rehovot 76100, Israel
[b] National Key Laboratory of Science and Technology on Advanced Composites in Special Environments, Center for Composite Materials and Structures, Harbin Institute of Technology, Harbin 150080, China

ARTICLE INFO

Keywords:
Monolayer
Ti_2C
MXene
Defect
Fracture
Toughness

ABSTRACT

MXenes, a novel class of monolayer transition metal carbides and nitrides, have gathered significant attention in materials science for their exceptional properties. This study focuses on investigating the influence of atomic defects on the fracture toughness of MXenes and similar monolayers. Comprehensive understanding and modeling of the fundamental physical mechanisms that govern MXene defect-mediated fracture is largely unexplored. Here, molecular dynamics simulations and theoretical fracture mechanics are employed to investigate the role of slit vacancy defects in the toughness of Ti_2C MXene. The material is found to exhibit brittle fracture behavior, and compared to classic predictions, its strength is significantly degraded by short defects. Two physical mechanisms are proposed to model MXene fracture — the material nonlinear elasticity, and the quantization of the crack driving energy. Combining both effects, this model is in excellent agreement with the MXene simulated toughness and may find application in other materials exhibiting similar toughness degradation and nonlinear elasticity.

1. Introduction

MXenes, a recently-introduced family of two-dimensional transition metal carbide and nitride atomic monolayers, attract considerable attention in materials science due to their remarkable properties, including high conductivity, excellent mechanical strength, and promising applications across various fields such as energy storage, coatings, nanocomposites and sensing devices [1]. At the same time, MXenes exhibit brittle behavior which makes them susceptible to flaws, a critical factor determining their structural integrity and reliability in practical applications [2].

Derived from the chemical exfoliation of 3D MAX phases (M - transition metal, A - metal, and X - carbon or nitrogen), MXenes are obtained through processes utilizing etchants like HF, HCL-LiF, and NH_4HF_2 [1]. Despite efforts to control reaction conditions, variability in wet solution chemistries often results in defects, layer irregularities, and structural misalignments within synthesized layers [1,3]. Structural reorganization during chemical etching, coupled with local chemical coordination, significantly impacts defect formation energy. MXenes exhibit lower carbon-vacancy formation energies compared to other 2D materials like graphene and MoS_2, which, combined with high migration energies, indicate stability of vacancy defects [4]. In other words, formation of vacancies is easier as the layer can stabilize more effectively even with missing atoms, and defects do not cause significant structural reconfiguration. The crystallite size and quality of the MAX phase also enable selective layer removal (precise removal of the A layers), affecting nanosheet integrity [3]. MXenes display complex fracture patterns due to their hexagonal atomic structure and intrinsic material orientations (armchair and zigzag), exhibiting anisotropic mechanical properties [2].

Atomic defects, including vacancies, grain boundaries, and surface terminations [5–8], are crucial for tailoring MXene-based materials to meet specific application requirements. Atom-vacancy defects are particularly significant, observed by atomic resolution STEM in synthesized MXenes [1]. The impact of vacancy defects on the toughness of 2D monolayers has been widely investigated by molecular dynamics, successfully predicting the atomic-scale fracture behavior [9–17]. Recently, these techniques have been applied to MXenes as well [2, 18–20], but these studies still lack theoretical description of the fundamental driving mechanisms. Hence, comprehensive understanding and modeling of how vacancy defects impact MXene fracture toughness remain elusive. We note that experimental investigation of such structures is not practical, nor is inducing slit defects of various lengths in real

---

* Corresponding authors.
E-mail addresses: green_is@netvision.net.il (I. Greenfeld), Linyang@hit.edu.cn (L. Yang), Daniel.Wagner@weizmann.ac.il (H.D. Wagner).
[1] These authors contributed equally to this work.

https://doi.org/10.1016/j.actamat.2025.120727
Received 1 October 2024; Received in revised form 17 December 2024; Accepted 8 January 2025

MXene monolayers, making investigation by molecular dynamics a viable and even necessary approach.

This paper presents a systematic investigation into the influence of MXene defects on fracture toughness, by inducing slit vacancy defects of varying lengths into the structure. Through molecular dynamics simulation [21] and theoretical fracture mechanics [22,23], we explore the structural evolution of a Ti_2C MXene under mechanical loading, emphasizing the role of defects in initiating and propagating fracture. This MXene type, comprising two layers of Titanium atoms engulfing a single layer of Carbon atoms, is deemed as representative of a wide variety of MXenes and monolayers. Exerting tensional load, while monitoring the local stress concentration at the defect tips and identifying fracture initiation, we obtain the material strength and its dependence on the defect length. Our theoretical modeling, which combines two physical mechanisms – nonlinear elasticity and energy quantization – offers fundamental understanding of MXene fracture mechanics.

2. Materials and methods

2.1. MXene and vacancy defects

The two-dimensional Ti_2C configuration was selected for molecular dynamics simulations as representative of monolayer MXene materials. Both armchair type and zigzag type chiralities were simulated. The Ti_2C monolayer sheets were approximately square, modeled with dimensions ranging from $15.10 \times 14.95\ \text{nm}^2$ to $172.56 \times 170.79\ \text{nm}^2$, depending on the defect length. The corresponding numbers of model atoms ranged from 8232 to 1075,072 (armchair defects) and 1075,104 (zigzag defects). Multi-vacancy defects were located near the center of the MXene nanosheets. A defect oriented in the armchair direction was termed 'armchair defect', whereas a defect oriented in the zigzag direction was termed 'zigzag defect'. Each nanosheet was over ten times larger than the induced defect to avoid edge effects [24], ensuring accuracy better than 0.5 % [25]. A supercomputer was employed for calculating the large models; the largest models of ~1M atoms took 60hr to calculate using 128 cores.

Being a solution-processible material, MXene may incur vacancy defects that remain stable after processing. Additionally, MXene may inherit inherent defects from the MAX-phase precursor [26]. These defects range from single, isolated vacancy defects to clusters of vacancies. They are commonly found in MXene structures, and have a significant impact on their mechanical properties [1]. In the simulation, we obtained the corresponding defect models by removing one or more atoms sequentially from the regular atomic sites in the crystal structure [27]. A wide range of defect lengths were implemented, from single vacancy to 128 vacancies, to examine the fracture behavior at long defects, approaching the behavior of a continuum, as well as at short defects of atomic scale, whose behavior deviates from continuum fracture mechanics.

During molecular dynamics simulations of two-dimensional materials with long, narrow induced defects, re-bonding can occur due to the close proximity of the defect surfaces. This can lead to unphysical defect closure or distortion of the stress field at the defect tip. In this study, the stabilization process for monolayer Ti_2C with elongated defects did not result in defect closure. However, in ultra-long defect models, interactions between the defect surfaces occurred, leading to distortions in the stress field at the crack tip. To prevent this, in the ultra-long defects ($n = 72, 96, 128$), overstressed atoms on the defect faces but far from its tips were removed to avoid generating undesired changes caused by the potential function.

The choice of linear slit defects, oriented perpendicularly to the load applied by middle tension, allows parametric analysis by varying the defect length, making it possible to obtain the intrinsic material toughness, as well as validation by known theoretical models of fracture mechanics. The applicability of fracture mechanics theories to atomic monolayers analyzed by molecular dynamics is elaborated and justified in Supplementary Note S4.

2.2. Molecular dynamics (MD) simulation

The large scale atomic/molecular massively parallel simulator (LAMMPS) [28] was used to perform the molecular dynamics simulations with the reactive force field [29]. The reactive force field is widely used to study the intra-plane and interlayer mechanical behavior of MXene and can accurately predict the deformation of MXene structures [7,19,30,31]. Refer to Supplementary Note S1 for validation of the effectiveness of reactive force fields in the analysis of Ti_2C mechanical properties, particularly its fracture toughness in the presence of embedded defects. This validation includes comparison to other MXene MD analyses, as well as to MXene DFT (Density Functional Theory) analyses.

Quasi-static relaxation of MXene nanosheets, using the conjugate gradient method prior to uniaxial tension, yielded a local energy minimum configuration with an energy tolerance of 1×10^{-10} kcal/mol and a force tolerance of 1×10^{-10} (kcal/mol)/Å. The MXene models were then fully relaxed under the NPT (conservation of matter, pressure, and temperature) ensemble at a temperature of 10°K for 50 ps to relieve the internal stresses in the structure and achieve a stable configuration. Finally, tensile loading was simulated under the NPT ensemble by applying a constant engineering strain rate of 10^{-6}/fs on a periodic box, by changing the dimension of the box in the stretching direction. The strain rate was applied just as a programming parameter, which does not induce a dynamic response in the simulated object. The simulated tensile loading used a time step of 0.2fs. The loading direction was perpendicular to the defects' length. The free open visualization tool (OVITO) was used to visualize the simulation results [32].

The tensile simulations were performed at a quasi-static temperature of 10°K to minimize the dynamic fluctuations of the structure. In order to obtain accurate stress field distributions at the atomic level, the structures were treated with the NVERE algorithm, which is a simple method for obtaining static equilibria of molecular systems using the micro-regular (NVE) ensemble [33]. The method enables more stable equilibrium configurations than conventional optimization algorithms, essential for studying the mechanical properties and deformation mechanisms of two-dimensional materials. NVERE minimizes the potential energy based on the NVE ensemble, and the model treated this way keeps its temperature around 0°K. We used low temperature in order to obtain accurate stress distributions and eliminate the effect of thermal fluctuations on the atomic-scale fracture of brittle materials. The stress-strain curves of defect-free MXene (Fig. 1b) demonstrate that, within the strain range below 10 %, temperature changes affect only marginally the mechanical response of the structure. When applying the maximum critical fracture stress criterion (see ahead), the critical fracture strain for most defective structures falls within the 10 % range, as shown in Supplementary Table S2. Therefore, the effect of temperature variations on the mechanical response of MXene with defects is expected to be minimal as well.

Supplementary Note S2 provides detailed description and justification for simulating at low temperature, an approach widely used to minimize thermal noise. That said, we realize that our simulation primarily reflects the intrinsic mechanical properties of MXene under idealized low-temperature conditions. The fracture stress and strain at higher temperatures require further studies for comprehensive evaluation. Therefore, as part of our future work, we plan to conduct additional simulations at a broader range of temperatures, including room temperature and higher, to more comprehensively understand the temperature effects on MXene mechanical behavior.

By spatially averaging the atomic stresses, an accurate map of the atomic stress distribution was obtained with a truncation radius of 3 Å. To calculate the stresses and moduli in the MXene, the thickness of the monolayer model was chosen to be 2.31Å (other thickness definitions

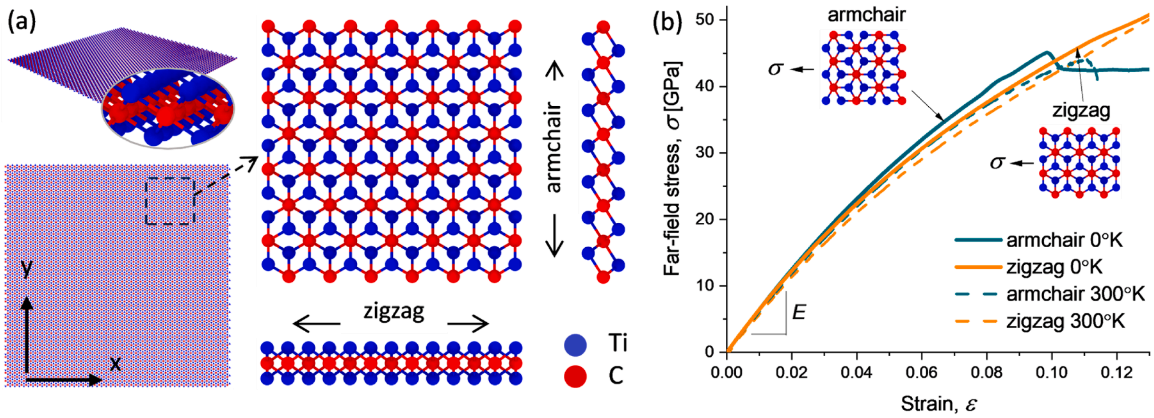

Fig. 1. Molecular dynamics Ti_2C MXene model. (a) Model structure and loading directions. (b) Elastic stress-strain curve of a pristine, defect-free model, at 0°K and 300°K, exhibiting nonlinear elasticity with initial elastic modulus *E*. The plot presents the low strain regime, which is of primary interest to this study (the high strain regime is shown in Supplementary Figure S4). The monolayer thickness used in calculating the stress and modulus is $t = 2.31$Å [18,34].

are also known in the literature) [18,34]. The maximum critical fracture stress of the Ti-C bond was determined from the available literature to be 60 GPa, and was used to determine whether the Ti-C bond at the defect tip exceeded the bond strength [5]. This criterion was used in the study to detect the initiation and propagation of MXene cracks and to evaluate the critical fracture state of defects of different lengths and orientations. Because of the way the potential function was implemented, this fracture criterion was not sufficient for generating spontaneous propagation. Therefore, once a bond exceeded its strength, it was discretely decomposed, and this was repeated multiple times to emulate propagation (see supplementary video). Spontaneous and continuous propagation was also validated by running the model without the use of a fracture criterion, demonstrating that after the first bond is broken, propagation continues relentlessly until complete fracture. The use of a maximum critical fracture stress criterion is justified in Supplementary Note S2, explaining how it resolves issues with the force field at high strains, with the selected specific value of 60 GPa obtained by DFT analysis of MXene.

3. Results and discussion

3.1. Ti_2C MXene and slit defects

The Ti_2C MXene is a two-dimensional monolayer, consisting of two external layers of Titanium (Ti) atoms and an internal layer of Carbon (C) atoms, bonded via Ti-C covalent bonds (Fig. 1a). Each carbon atom is bonded to six titanium atoms, whereas each titanium atom is bonded to three carbon atoms. The MXene is not isotropic and its properties are dependent on the chirality direction, of which we chose to explore the principal chiralities - armchair (AC) and zigzag (ZZ). To analyze its fracture behavior in the presence of defects, the Ti_2C was modelled and simulated by molecular dynamics (MD), applying unidirectional uniform strain at constant rate to the model. The simulation was validated by running a pristine, defect-free Ti_2C model (Fig. 1b), yielding an average modulus of about 630 GPa and an average strength (far-field stress at fracture) of about 50 GPa, in line with the literature [2,7,35]. See materials and methods for definitions and details.

The MXene elastic behavior is nonlinear, a material property that has a significant impact on the fracture toughness, to be shown later. We use the empirical Ramberg-Osgood equation [22,36] to fit the stress-strain curve in the elastic range, using the following form:

$$\varepsilon = \frac{\sigma}{E}\left[1+\alpha\left(\frac{\sigma}{\sigma_0}\right)^m\right] \tag{1}$$

where σ is the far-field (applied) stress, *E* is the modulus (slope at the origin), σ_0 is a reference stress, α is a dimensionless constant, and *m* is a strain hardening/softening exponent. The parameters α, σ_0 and *m* determine the degree of nonlinearity. Fitting Eq. (1) to the data obtained by the simulation we get $m = 2 \pm 0.1$, with α fixed at 1 to avoid over-parameterization (two independent parameters are sufficient for that equation [22]). Setting $m = 2$ in order to simplify the modeling, the calculated fitting parameters are $E = 637$ and 623 GPa and $\sigma_0 = 72.8$ and 66.1 GPa for armchair and zigzag loading directions, respectively ($R^2 > 0.9999$). These moduli and stresses are calculated at 0°K temperature, whereas at 300°K they are slightly lower (see materials and methods, and justification in Supplementary Note S2).

Slit defects of gradually increasing length were induced in the model, in both armchair and zigzag chiralities, and were simulated under load (Fig. 2a). The model size is at least 10 times larger in each direction than the defect length, to avoid geometrical edge effects on the stress field [11–13]. The defects are vacancy defects, created by alternating removal of Ti and C atoms in the following sequence: front-layer Ti (defect designated by 1ti), C (1ti1c), back-layer Ti (2ti1c), C (2ti2c), and repeating this sequence until four Ti atoms and four C atoms are removed (4ti4c) (Fig. 2b). Longer defects up to 64ti64c were also simulated (Fig. 2c). See details in materials and methods.

The straight cracks formed in this way are positioned perpendicularly to the stress direction, such that an armchair defect is tensioned in the zigzag direction (Fig. 2b and c upper rows), and a zigzag defect is tensioned in the armchair direction (Fig. 2b and c lower rows). Armchair defects can alternatively be induced by a different removal sequence to avoid the small bulges in the defect's right face, but this would entail skipping the removal of every second C atom in the sequence and was therefore not used. Although the simulated defects may not necessarily appear as such in actual MXenes, they allow thorough analysis of the MXene fracture toughness over a wide range of defect sizes, as well as comparison and validation by fracture toughness theory and known models. As will be shown later, while the toughness in the presence of long defects conforms to linear elastic fracture mechanics (LEFM), short defects significantly degrade the toughness compared to LEFM prediction.

The fracture toughness is determined from the strength dependence on defect length. Thus, the defect length is a key parameter in the analysis, and, because the defect is induced by sequential removal of atoms, its length is a discrete function of the number of missing atoms. To obtain this function we observe the repeating unit cell and defect dimensions defined in Fig. 3a and b. In the case of a zigzag defect, each removed atom, whether Ti or C, adds a distance *h* to the defect length. In the case of an armchair defect, each removed atom adds a distance *l* to the defect length, except when a removal of a C atom is not in line with the defect main axis where only $\frac{l}{2}$ is added, occurring once every four atom removals. This leads to the following functions of the defect half-

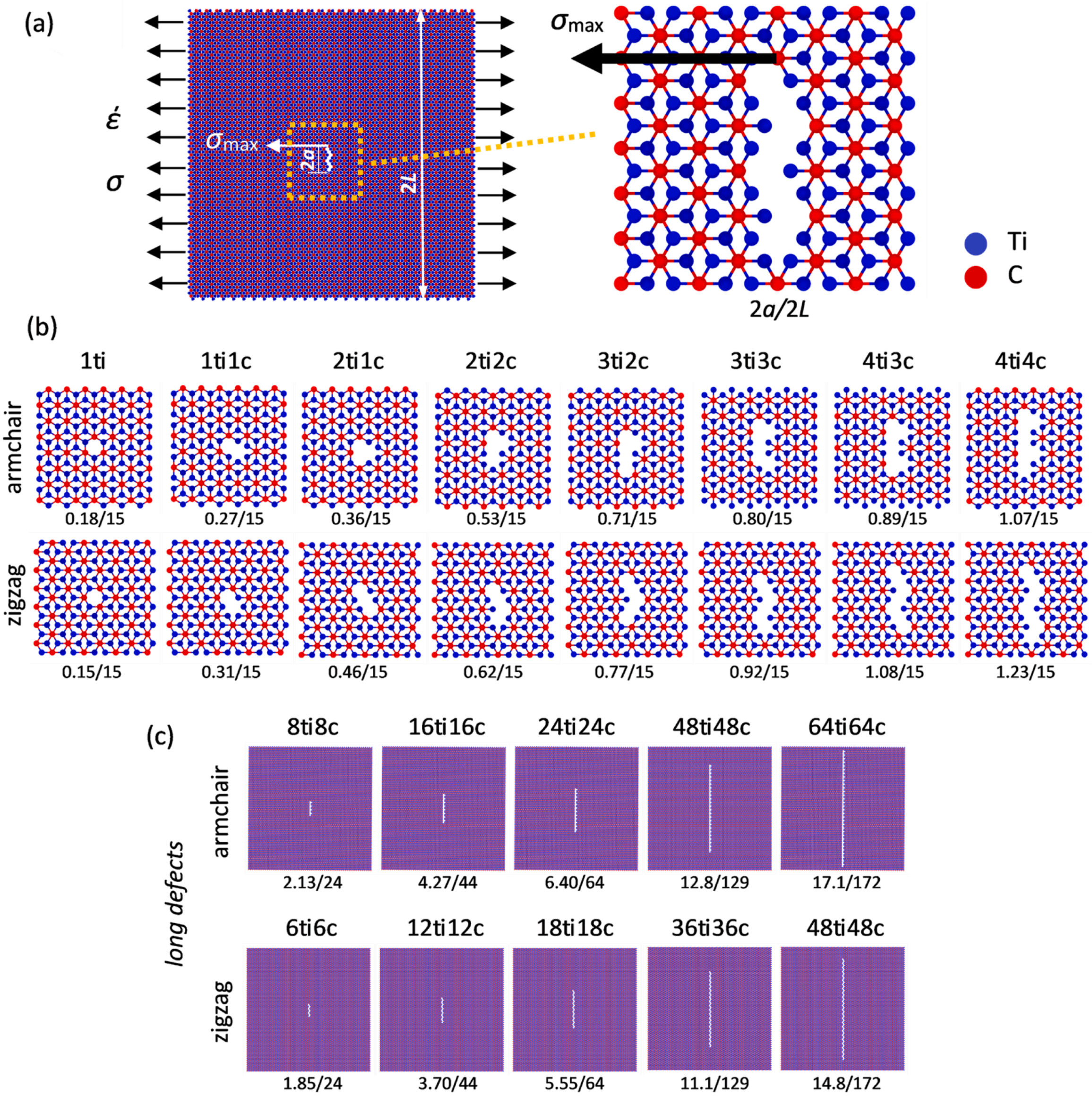

Fig. 2. Defect types and loading. (a) Loading at strain rate $\dot{\varepsilon}$ with far-field stress σ perpendicular to the defect length. The maximum local stress σ_{max} occurs at the defect tip. The model size $2L$ in each direction is at least 10 times the defect length $2a$. (b.c) Simulated defects oriented in armchair and zigzag directions, designated by the number of missing Ti and C atoms. The defect length and model size (nm), $2a/2L$, are denoted below each configuration.

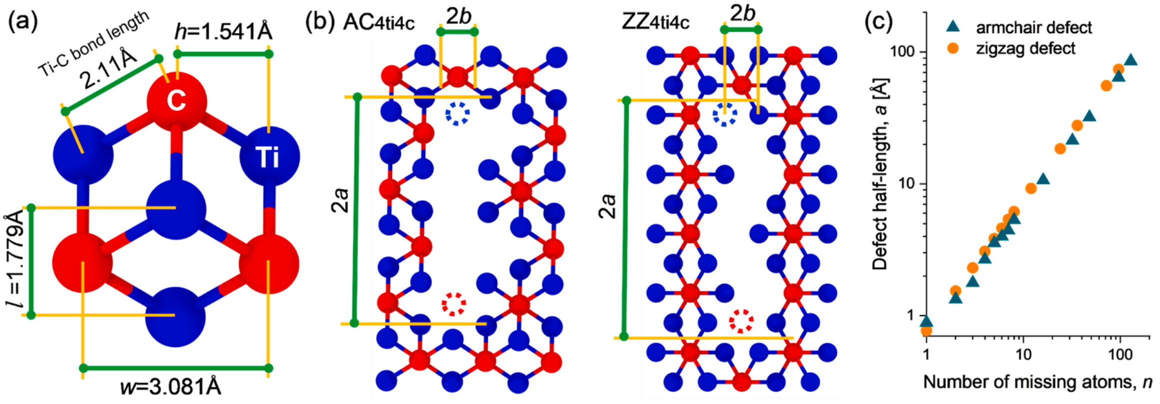

Fig. 3. Defect dimensions. (a) Dimensions in a Ti_2C unit cell. (b) Definition of the defect length $2a$ and width $2b$. The dotted circles are the missing atoms closest to the defect tips. The defect length is shorter than the distance between the end atoms by $l = 1.78$Å (armchair) and $h = 1.54$Å (zigzag). This definition ensures that $2a = 0$ in a defect-free model. (c) Length of defects used in the simulation vs. the number of missing atoms (vacancies) n in each defect.

length a with respect to the number of missing atoms (that is, atom vacancies) n:

$$a_{AC} = \frac{l}{2}\begin{cases} \frac{3n}{4}, & \bmod\left(\frac{n-2}{4}\right) = 0 \\ n - \left\lfloor \frac{n+1}{4} \right\rfloor, & \text{otherwise} \end{cases} \tag{2}$$

$$a_{ZZ} = \frac{h}{2}n$$

The subscripts AC and ZZ stand for armchair and zigzag defects, respectively. The condition with the mod function is used to denote the terms $n = 2, 6, 10..$, where the C atom removal is off the defect's main axis (seen in Fig. 3b); the mod function provides the remainder – the integer left-over remaining from integer division, e.g., for $n = 6$ it is 0 and the condition is met, whereas for $n = 11$ it is 1 and the condition is not met. The floor function $\lfloor x \rfloor$ (greatest integer less than or equal to x) is used for the length of the other terms, where the C atom removal is inline. This definition ensures that in a defect-free model ($n = 0$) the defect length will be zero as required. The armchair function yields a sequence $a_{AC} = \frac{l}{2}(0,\ 1,\ 1.5,\ 2,\ 3,\ 4,\ 4.5,\ 5,\ 6..)$ for $n = 0,1,2..$, which can be verified on the model geometry. The defect half-width b is constant, given by $b_{AC} = \frac{h}{2} = 0.771$Å and $b_{ZZ} = \frac{l}{2} = 0.890$Å, which vanishes in a defect-free model. The length of the simulated defects is depicted in Fig. 3c as function of the number of missing atoms.

3.2. Stress concentration and crack propagation

The stress distribution in a defected model under uniaxial tension is not uniform, and stress concentration appears at the defect tips. The example in Fig. 4a shows a model with an armchair defect, under a uniform horizontal tensile load of about 31.9 GPa, while the stress at the defect tips amounts to 60 GPa. The stress map is characteristic of defects in continuum solids, with elevated stress at the defect tips (red atoms) while low stress across the defect gap (blue atoms), much lower than the far-field stress and close to 0 GPa. The fracture condition used in the simulation is when the local maximum stress $\sigma_{\max}$ exceeds the ultimate (fracture) stress of $\sigma_u = 60$ GPa (see details in materials and methods, and justification in Supplementary Note S2) [5]. An exclusion to this criterion occurs in armchair loading of the pristine model and the 1ti zigzag defect (but not in longer zigzag defects), which start yielding (Fig. 1b) at a local stress of 57 GPa instead of 60 GPa.

A remarkable observation is the stress nonuniformity far from a defect, as seen in the magnification (Fig. 4a, circular inset): the average stress in a carbon atom (~43 GPa) is higher than in a titanium atom (~27 GPa). As a result, in a pristine model, the fracture criterion is reached at a far field stress lower than 60 GPa: in armchair loading direction 49.6 GPa (strain 0.18), and in zigzag loading direction 51.0 GPa (strain 0.13). The reason for this nonuniformity is the Ti_2C triple layer of atoms, with carbon atoms in the middle and titanium atoms on top and bottom, which, to maintain equilibrium in its free state, sustains internal stresses. This molecular configuration is different from single-layer atomic structures such as graphene. When pristine graphene is analyzed using the same fracture criterion, the stress distribution is uniform, and the far-field stress is the same as the maximum stress. By contrast, in the Ti_2C model before loading, the atoms bear tensile or compressive prestresses, different for each atom type whether Ti or C, and different in each of the three directions. Such prestresses were also reported by other MXene MD simulations [30]. Thus, although the Ti and C atoms incur the same stress increment under load, its superimposition over their different prestresses results in an inhomogeneous stress field and consequently weakening of the strength.

These prestresses are also a likely contributor to the Ti_2C nonlinear elasticity, as are the intrinsically nonlinear interaction between the Ti and C atoms [2]. Atomic prestresses result from the interactions between atoms, involving changes in atomic positions and interatomic forces, and can cause deviations from linear elastic behavior. These local distortions and forces can affect the overall material response to stress and strain, leading to nonlinear elasticity. We see this nonlinearity within our region of interest, up to about 10 % strain (Fig. 1b), and therefore it is unlikely the result of large deformations. When an external stress is applied on a structure with internal prestresses, the local stress is a superposition of the applied stress and the prestress, whether positive or negative. As the external tension stress is increased, the local stress at an atom with a tensile prestress initially rises moderately until the prestress is completely overcome, and then rises at a higher rate (see example in Supplementary Note S8), whereas the local stress at an atom with a compressive prestress initially rises steeply until the prestress is

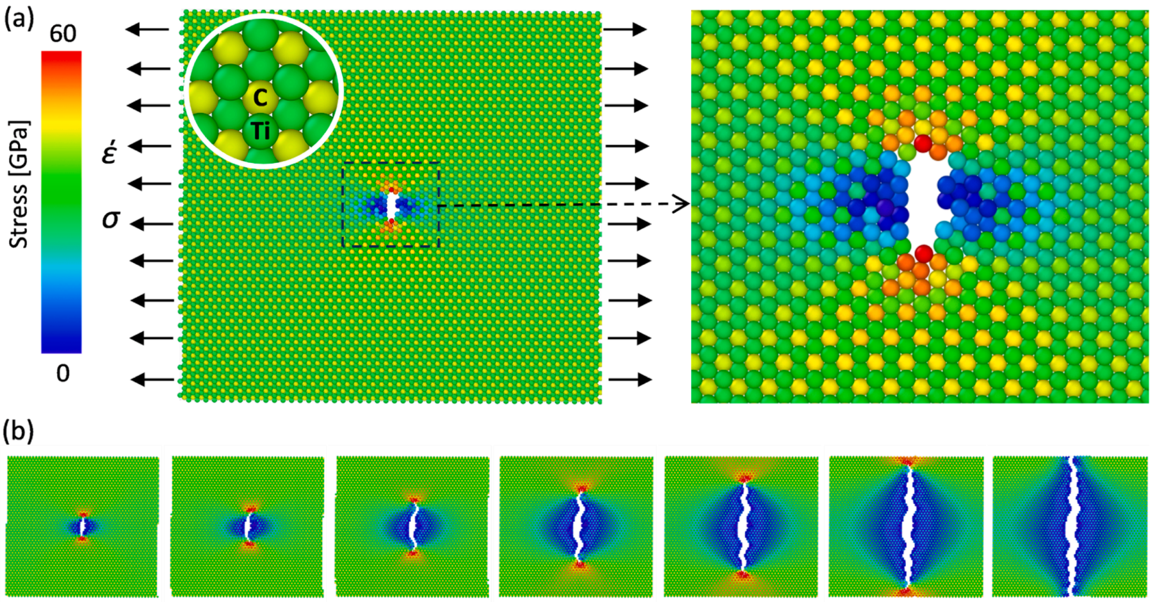

Fig. 4. Local stress and crack propagation. (a) Nonuniform stress distribution around a typical defect, peaking at the defect tips to 60 GPa (the fracture strength criterion). The circular inset zooms in on a region far from the defect, exhibiting stress nonuniformity. (b) Spontaneous crack propagation, induced by removing Ti-C bonds which exceed the fracture strength.

completely overcome, and then rises at a moderate rate. The resultant effect in the Ti_2C structure is larger stress-strain slope (elastic modulus) at low strain, and smaller slope at high strains. The degree of nonlinearity (Eq. (1), parameters m and σ_0) is affected by the prestress fields and bonds elasticity in the MXene structure.

When the maximum local stress exceeds the fracture stress, a crack starts propagating spontaneously from the defect tips. Crack propagation was simulated at a slowly increasing far-field load by dissociating over-stressed bonds without creating new ones. The crack propagates continuously until complete rupture of the model (Fig. 4b and Supplementary GIF animation file), a failure behavior characteristic of brittle materials. The driving force for this propagation is the increasing stress concentration at the tips of the crack as it grows. In terms of fracture mechanics, the energy released in the regions across the crack gap (blue regions) grows with the crack growth and is dissipated by the fracture energy needed to break bonds. See more details about the propagation simulation in the materials and methods section. The conditions for an unstable defect, which may develop into a crack propagating until failure, are analyzed by J integral analysis in Supplementary Note S5.

During the simulation, the stress field was continually monitored, and fracture was identified when the stress at the edge of a defect, $\sigma_{\max}$, exceeded the fracture criterion of $\sigma_u = 60$ GPa. The far-field stress at that point, σ_f, is the model strength, depicted in Fig. 5a for all tested models. Stress concentration is defined as the ratio between the maximum local stress and the far field stress. Because the model's elasticity is nonlinear (Fig. 1b and Eq. (1)), the stress concentration is not constant but depends on the applied stress, and therefore we specify it at $\sigma = \sigma_f$:

$$K_t = \frac{\sigma_u}{\sigma_f} \tag{3}$$

depicted in Fig. 5b and c. Note that K_t of a pristine model is not exactly 1, as might be expected, but a little higher because of the stress nonuniformity in the unloaded structure as described above.

Stress concentration at the tip of a long defect generally depends on the defect length $2a$ and the tip radius ρ. For an elliptically-shaped defect in a plate, the stress concentration was calculated by Inglis [37]:

$$K_t = 1 + 2\sqrt{\frac{a}{\rho}} \tag{4}$$

This expression can also be used as an approximation for oblong non-elliptical defects of length $2a$ and tip radius ρ to a reasonable accuracy (equivalent-ellipse approximation) [37,38]. For sharp defects, this prediction unrealistically diverges, an outcome that drove Griffith to develop his energy-based model for fracture, to be detailed in the next section. However, the tip of an MXene defect is neither circular (Fig. 3b), nor is it sharp. The best that can be done is to try fitting Eq. (4) to the MXene MD simulation results (Fig. 5c, dashed lines). We see a reasonable fit for long defects, implying that long defects behave similarly to defects in a continuum solid, but somewhat poorer fit for short defects. Furthermore, the calculated fitting parameter is $\rho \cong 18$Å (but larger, 28Å, when fitting just the short length region), a large radius indeed compared to the atomic radius of 2.1Å (Fig. 3a, bond length) or the defect half-width b. We may infer that (i) Inglis model overestimates the stress concentration in short defects, and (ii) the Ti_2C defect tip is blunt. A better fit can be derived from fracture mechanics (Fig. 5c, solid lines, Eq. (17)), as described in the following section.

3.3. Fracture toughness

The theory of fracture mechanics replaces the stress concentration approach by energy balance as a criterion for fracture, avoiding the theoretical stress divergence at the tip of an infinitesimally sharp crack. The usage of fracture mechanics in the analysis of atomic monolayers analyzed by molecular dynamics is elaborated and justified in Supplementary Note S4. Thus, a crack will propagate when its growth releases an amount of elastic energy sufficient to overcome the fracture energy (the energy to dissociate bonds across the crack faces). For linear elasticity, the elastic energy released by a cracked plate (blue low-stress regions in Fig. 4), calculated by Inglis [37] and used by Griffith [39], is given by (plane stress) [22]:

$$U_e = \left(2\pi a^2 B\right)\left(\frac{\sigma^2}{2E}\right) \tag{5}$$

where the term $\sigma^2/2E$ is the elastic energy density in these regions prior to the presence of a crack, and the term $2\pi a^2 B$ denotes the volume of these regions ($2\pi a^2$ is equivalently the area of two triangles, each with base $2a$ and height πa, and B is the plate thickness). The fracture energy, on the other hand, is $U_s = 2aBG$, where G is the cohesive fracture energy per unit crack area (see calculation example of G in Supplementary Note

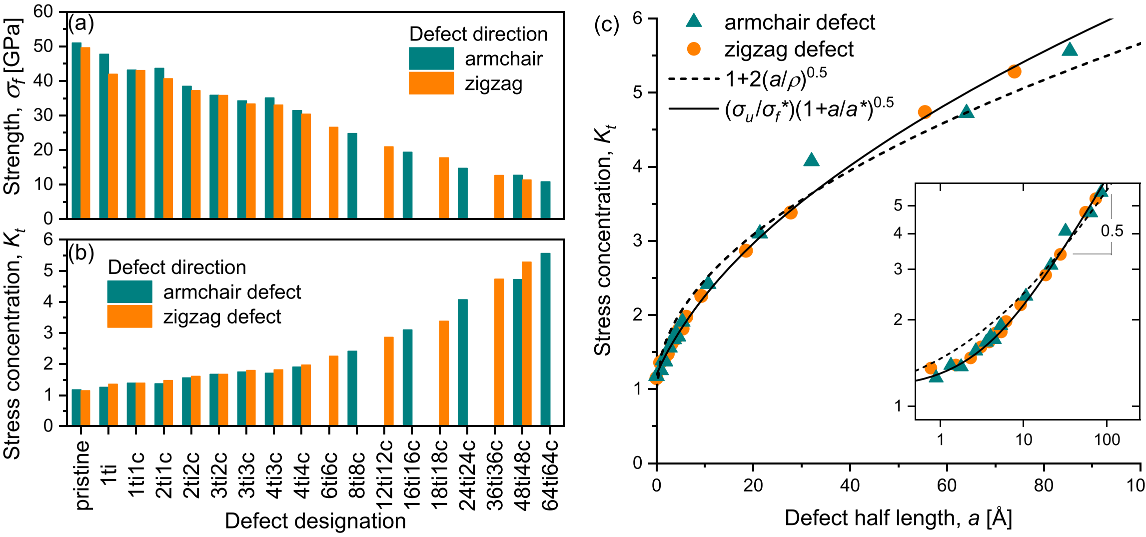

Fig. 5. Strength and stress concentration. (a,b) Strength and stress concentration for the simulated defected models. The defect designation indicates the number of removed atoms in each atom type. (c) Stress concentration vs. defects half-length, and theoretical trendlines (only zigzag lines are shown, to avoid clutter). The inset is a log-log plot of the same data. The dashed-curve is a fit to Eq. (4) (Inglis) ($\rho_{AC} = 17.9$Å and $\rho_{ZZ} = 18.4$Å, $R^2 > 0.97$). The solid curve is a fit to Eq. (17) (fracture mechanics) ($\sigma_u/\sigma_f^* = 1.15$, $a^* = 3.51$Å, $R^2 > 0.99$), much better than the Inglis fit.

S6). Griffith energy balance is obtained by equating the change in these energies due to an incremental change in crack area, $dU_e/dA = dU_s/dA$, where $A = 2aB$ is the crack area. The first derivative is known as the energy release rate, $\mathscr{G}$. Solving for the fracture stress:

$$\sigma_f = \sqrt{\frac{EG}{\pi a}} = \frac{K_{Ic}}{\sqrt{\pi a}} \tag{6}$$

where $K_{Ic} = \sqrt{EG}$ is the material fracture toughness (mode I).

This classic solution applies to linear elastic fracture mechanics (LEFM). It is depicted in Fig. 6 (thin solid lines) against the simulation results, and shows convergence to the data at very long defects ($K_{Ic} =$ 1.67 and 1.71 MPa·m$^{0.5}$ for armchair and zigzag defects, respectively), but rather poor prediction (strength over-estimation) for defects of half-length below about 20Å. This deviation is best seen in the log-log plot (Fig. 6b), and, as will be described, can be attributed to the nonlinear elasticity of the Ti_2C MXene and the quantization of the released elastic energy. A cross-check of these fracture toughness values is obtained by calculating the energy to remove an atom at the edge of a defect, representing a small incremental growth of crack length (see Supplementary Note S6).

When the elasticity is nonlinear, as is the case with the Ti_2C MXene, the elastic energy density stored prior to the presence of a crack is obtained by integrating the area underneath the stress-strain curve (Fig. 1b). Thus, the elastic energy released by a cracked plate is given by:

$$U_e = v_e \int_0^{\varepsilon} \sigma d\varepsilon = 2\pi a^2 B \frac{\sigma^2}{2E}\left[1 + 2\alpha\frac{m+1}{m+2}\left(\frac{\sigma}{\sigma_0}\right)^m\right] \tag{7}$$

where v_e is the volume from which the elastic energy is released (blue regions in Fig. 4a), approximated by the volume used in linear elasticity, $2\pi a^2 B$. The integral is the elastic energy density, calculated by change of variables, $\int_0^{\varepsilon} \sigma d\varepsilon = \int_0^{\sigma} \sigma\left(\frac{d\varepsilon}{d\sigma}\right) d\sigma$, where $d\varepsilon/d\sigma$ is obtained by deriving Eq. (1) with respect to σ. This solution applies to nonlinear elastic fracture mechanics (NLFM). In a nonlinear elastic material v_e may depend on the stress, as regions of high stress have different stiffness (lower in the MXene case) than regions of low stress. To simplify the analysis, we assumed in the equation above that this stress dependency is incorporated in the nonlinearity term in brackets, and will be reflected in the fitting to the simulated strength data. We see that in NLFM the energy released for driving the crack is larger than the energy in LEFM (Eq. (5)) due to the factor in brackets, reducing the toughness. In other words, the stiffness at fracture at high stress (short defects) is smaller than that at low stress (long defects) (the slope of the stress-strain curve at high stress is smaller, Fig. 1b), and therefore the elastic energy density, which is inversely dependent on the modulus, is larger. The nonlinearity effect is higher for larger values of the ratio σ/σ_0, that is at high stress.

The elastic nonlinearity is not expected to affect the fracture energy $U_s = 2aBG$. The energy balance is obtained by equating the change in the elastic and fracture energies with respect to an incremental crack growth, $dU_e/dA = dU_s/dA$. The first derivative is known as the nonlinear energy release rate, J, or J contour integral, for which $J = \mathscr{G}$ is the special case of linear elasticity. Solving for the critical crack length:

$$a = \frac{EG}{\pi\sigma_f^2\left[1 + H\left(\frac{\sigma_f}{\sigma_0}\right)^m\right]}, \quad H = 2\alpha\frac{m+1}{m+2} \tag{8}$$

This expression yields the strength dependence on crack length, and is validated by J integral analysis in Supplementary Note S5, including crack instability analysis. For the MXene analyzed in this study ($m = 2$, $\alpha = 1$ and hence $H = 3/2$), an instructive approach is to simplify Eq. (8) by applying a series expansion approximation to the term in brackets:

$$a \cong \frac{EG\left[1 - \frac{3}{2}\left(\frac{\sigma_f}{\sigma_0}\right)^2\right]}{\pi\sigma_f^2} \cong \frac{EG}{\pi\sigma_f^2} - \frac{3EG}{2\pi\sigma_0^2} \tag{9}$$

The accuracy of this approximation is of order $O\left(\left(\sigma_f/\sigma_0\right)^4\right)$ (that is, the magnitude of the next term in the expansion), better than 10 % for typical actual values of σ_f (Fig. 5a) and σ_0 (Eq. (1), $\sigma_f \ll \sigma_0$); the accuracy may be further improved by fitting the constant second term to the simulation data. Solving for the fracture stress:

$$\sigma_f \cong \frac{K_{Ic}}{\sqrt{\pi(a+p)}}, \quad \text{where } p = \frac{3EG}{2\pi\sigma_0^2} = \frac{3K_{Ic}^2}{2\pi\sigma_0^2} \tag{10}$$

The value of the constant nonlinearity term p is 3.05Å for armchair defects and 2.63Å for zigzag defects, and its effect is to reduce the strength (fracture stress) at short defects. We note that p is constant only

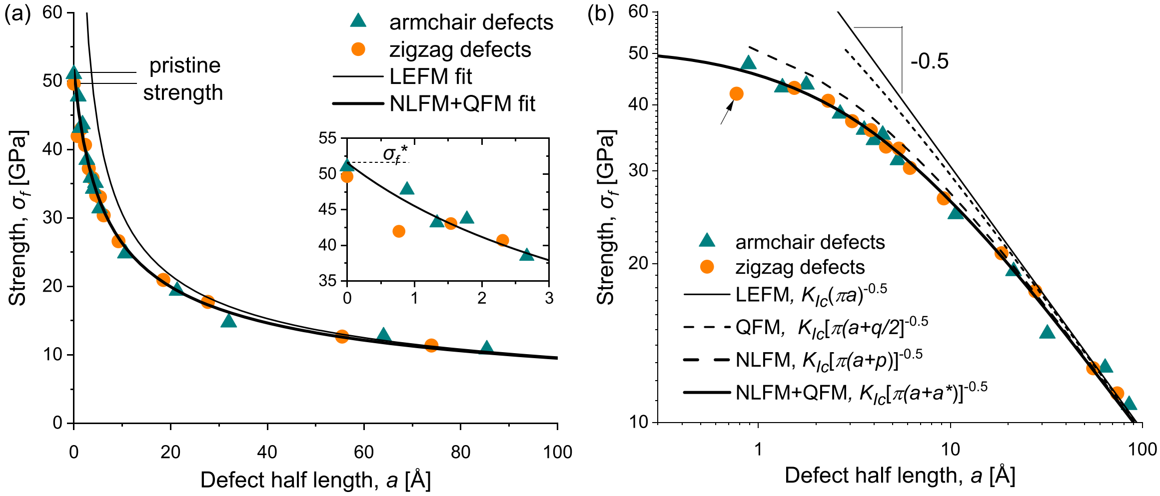

Fig. 6. Simulated strength and fracture modeling. Strength of armchair and zigzag defected models tensioned perpendicularly to the defects length vs. the defects half-length, and theoretical trendlines (only zigzag lines are shown, to avoid clutter). The NLFM+QFM curve is fitted to the data with fracture toughness $K_{Ic} = 1.67$ and 1.71 MPa·m$^{0.5}$ and $a^* = 3.22$ and 3.51Å ($R^2 > 0.99$) for armchair and zigzag defects, respectively. The QFM curve is depicted for fracture quantum $q = 1.33$ and 1.54Å calculated by Eq. (13). The NLFM curve is depicted for nonlinearity parameter $p = 3.05$ and 2.63Å calculated by Eq. (10). (a) Linear-linear plot. The magnification (inset) shows the prediction for the pristine strength, σ_f^*. (b) Log-log plot. The arrow marks a single case that yielded prior to breaking. Acronyms: LEFM – linear elastic fracture mechanics, NLFM – nonlinear fracture mechanics, QFM – quantized fracture mechanics.

for $m = 2$ (the exponent in Eq. (1)), when the elastic nonlinearity can be approximated by it, otherwise it is a function of σ_f. This solution is depicted in Fig. 6b (NLFM, long-dashed line) and agrees much better with the simulation results compared to LEFM, but still slightly deviates from the data at short defects.

To resolve this deviation, we apply the theory of quantized fracture mechanics (QFM) developed by Pugno and Ruoff [23]. QFM assumes quantization of the LEFM fracture criterion, attributed to the discrete propagation of a crack in an atomic-scale structure such as the MXene, and consequently discrete strain-release energies. In LEFM the stress intensity factor in a cracked plate is a continuous function of the crack length, $K_I(a) = \sigma\sqrt{\pi a}$. However, in an atomic-scale structure the length of the crack is a discrete function of the number of vacancy atoms. To recover continuity, the stress intensity factor is averaged over a distance of atomic scale, q, termed the fracture quantum. Thus [23]

$$K_{Ic} = \sqrt{\frac{1}{q}\int_a^{a+q} K_I^2(a)da} = \sigma\sqrt{\pi(a+q/2)} \tag{11}$$

and the fracture stress is

$$\sigma_f = \frac{K_{Ic}}{\sqrt{\pi(a+q/2)}} \tag{12}$$

The fracture quantum can be estimated by the discrete step in defect length per each atomic vacancy [23]. Using Eq. (2), the following estimate is obtained:

$$q = \frac{2a}{n} = \begin{cases} \dfrac{3l}{4} = 1.33\text{Å armchair defect} \\ h = 1.54\text{Å zigzag defect} \end{cases} \tag{13}$$

The QFM quantization effect is a reduction in the strength (fracture stress) at short defects, similar to the NLFM effect but much smaller. This solution is depicted in Fig. 6b (short-dashed line) and deviates significantly from the data at short defects. QFM also offers a correction of the fracture toughness for blunt cracks, described in Supplementary Note S7.

The strength expressions in NLFM (Eq. (10)) and QFM (Eq. (12)) are similar in form, suggesting that the values of p and $q/2$ imposed on a are additive. Therefore, we may write a combined expression of both theories:

$$\sigma_f = \frac{K_{Ic}}{\sqrt{\pi(a+a^*)}} = \frac{\sigma_f^*}{\sqrt{1+\frac{a}{a^*}}}, \text{ where } a^* = p + q\Big/2 \tag{14}$$

where σ_f^* is the MXene pristine strength (that is, the far-field stress at failure, Eq. (15)). The term a^* is a material property, which depends on the material nonlinearity (through p) and the discreteness of the atomic structure (through q), both inherent properties of the MXene. This equation is fitted to the simulation data in Fig. 6a and b (thick solid lines) with good agreement, where a^* served as the fitting parameter, yielding 3.22Å for armchair defects and 3.51Å for zigzag defects.

3.4. Pristine strength

The predicted pristine (that is, defect-free) strength is obtained when $a = 0$ (Eq. (14)):

$$\sigma_f^* = \frac{K_{Ic}}{\sqrt{\pi a^*}} \tag{15}$$

indicated in Fig. 6a (inset) and close to the simulated strengths. Unlike LEFM, the strength prediction when NLFM and QFM are combined does not diverge when there is no defect, making this fracture mechanics approach more realistic than LEFM.

As noted, the term a^* is a material property, but what is its significance? We have shown that it comprises two variables, the nonlinearity term p and the fracture quantum q. In the case of the Ti_2C MXene, the effect of the nonlinearity on fracture toughness is predominant over that of the quantization, particularly in a structure with short defects (see Fig. 6b). Quantization is relevant for atomic-scale structures, with defects of atomic scale, but its effect vanishes in micro-scale or macro-scale structures where harmful defects are typically micro-sized or larger (that is, $a \gg q$). By contrast, nonlinearity has an effect on fracture toughness at all scales, such that high nonlinearity (small σ_0 leading to large p, Eqs. (1) and (10)) tends to reduce the strength of a structure with short defects. NLFM as formulated in Eq. (8) still ‘suffers’ from the unrealistic divergence of the strength for infinitesimal cracks and pristine structures, but the expression in Eq. (10) seems to avoid this divergence even though it is a result of an approximation. Be that as it may, the combination of NLFM and QFM delivers good predictions for the finite strength of the pristine MXene (Eq. (15) and Fig. 6a, inset).

Following these thoughts, in a nonlinear elastic, brittle material that is free of defects, fracture mechanics as formulated in Eq. (10) may provide the material finite strength, rather than diverging strength as in LEFM. Thus, at size scales above atomic scale, where quantization may be neglected, the pristine strength may possibly be related to nonlinearity by:

$$\sigma_f^* \cong \sqrt{\frac{2}{3}}\sigma_0 \tag{16}$$

where p from Eq. (10) was substituted into Eq. (15). σ_0 is inversely related to the degree of nonlinearity, so that material with large σ_0 is closer to linear elasticity, whereas material with small σ_0 is closer to nonlinear elasticity. In other words, the more linear a material is, the higher its pristine strength, and vice versa. This is a remarkable prediction, which relates the pristine strength of nonlinear elastic materials to just the degree of nonlinearity. An example of such nonlinear elastic material is amorphous silica, a brittle material [40]. The physical rationale behind this relation is the likely effect of prestresses, discussed in detail in the stress concentration section, which contributes simultaneously to nonlinearity and to strength reduction.

The QFM theory suggests that NLFM and LEFM are both limit cases of QFM [23]. This is indeed implied in Eq. (12), such that when setting $q = 2p$ it reduces to NLFM and when setting $q = 0$ it reduces to LEFM. QFM further suggests that for scales larger than the atomic scale, the fracture quantum could be derived from the material strength, $q = 2K_{Ic}^2/\left(\pi\sigma_f^2\right)$ (Eq. (12) with $a = 0$), and thus may have values larger by several orders of magnitudes than the atomic scale; so, ‘finite crack extension’ would be a more appropriate term than ‘fracture quantization’ [23]. However, both suggestions are more phenomenological than analytic, as they extend the scope of the fracture quantum away from its fundamental physical meaning, as well as presuppose prior knowledge of the strength and fracture toughness from experiments or simulations. More about this further on.

3.5. Stress concentration relation to fracture toughness

The finite strength of the MXene, provided by the combined NLFM and QFM theory, and the finite stress concentration at the defect tip, imply a relation between the fracture toughness and the stress concentration. Substituting Eq. (14) in (3):

$$K_t = \frac{\sigma_u}{K_{Ic}}\sqrt{\pi(a+a^*)} = \frac{\sigma_u}{\sigma_f^*}\sqrt{1+\frac{a}{a^*}} \tag{17}$$

This expression is depicted in Fig. 5c (solid lines) with good fitting to the simulation data, much better than the fit to Inglis equation (equivalent-ellipse, Eq. (4)). The term $\sigma_u/\sigma_f^* \geq 1$ is the ratio between the ultimate local stress (the fracture criterion) and the strength of the pristine, defect-free structure, both material properties as they are invariant with respect to shape and size. We would have expected this ratio to be equal to 1, were it not for the inherent prestresses in the MXene structure at free state, as explained before; these prestresses cause local stress concentrations, which account for the simulated initial stress concentration ($K_{t0} > 1$) in a defect-free MXene (Fig. 5b and c).

The square-rooted term is different from Inglis stress concentration equation. For very long defects, the stress concentration converges to $K_t \cong \frac{\sigma_u}{\sigma_f^*}\sqrt{\frac{a}{a^*}}$, compared to $K_t \cong 2\sqrt{\frac{a}{\rho}}$ for the equivalent-ellipse approximation, both proportional to the square root of the defect length, but with different prefactors: whereas the prefactor for the ellipse approximation is purely geometric, the prefactor in the fracture mechanics expression depends on three material properties σ_u, σ_f^* and a^* (see also the correction for blunt cracks in Supplementary Note S7, which introduces ρ into QFM). This is a more complex view of the concept of stress concentration, which, beyond geometry, considers the initial stress concentration due to inherent prestresses, the material nonlinearity, and the quantization at the atomic scale.

3.6. Comparison to other materials

Here, we compare the fracture toughness K_{Ic} of Mxene to other materials. Evidently, K_{Ic} by itself is not sufficient for describing the material fracture toughness, and must be combined with the nonlinearity+quantum term a^* (Eq. (14)) to fully describe the material strength in the presence of a defect. However, a^* values are currently not available in the literature, and therefore our comparison is limited to K_{Ic}, representing the fracture toughness in the presence of long defects where a^* is negligible with respect to a.

The fracture toughness K_{Ic} of the Ti_2C MXene is found by strength fitting to be 1.67 $MPa{\cdot}m^{0.5}$ (armchair defects) and 1.71 $MPa{\cdot}m^{0.5}$ (zigzag defects) (Fig. 6). Slightly higher values (2.15 and 2.10 $Mpa{\cdot}m^{0.5}$) are predicted by using bond dissociation energies (see Supplementary Note S6). These values are about the same as glass ceramic (1.4–1.7 $Mpa{\cdot}m^{0.5}$), higher than silica glass (0.6–0.8 $Mpa{\cdot}m^{0.5}$), and moderately lower than typical carbides (2–5 $Mpa{\cdot}m^{0.5}$) and alumina (3.3–4.8 $Mpa{\cdot}m^{0.5}$) [41]. In that sense, the MXene belongs to the class of moderately brittle materials. A similar MD study on Ti_2C resulted in higher values (most probably due to different fracture criterion and thickness definition), about 4.8 $MPa{\cdot}m^{0.5}$ (armchair) and 6.0 $MPa{\cdot}m^{0.5}$ (zigzag), using the moduli and fracture energies in the expression $K_{Ic} = \sqrt{EG}$, and even higher values for Ti_3C_2 [2]. Comparing to other monolayer structures, the fracture toughness of graphene was found to be about 2.8 $MPa{\cdot}m^{0.5}$ [9], and that of single-wall CNT 2.5–2.9 $MPa{\cdot}m^{0.5}$ [10], somewhat higher than the MXene, possibly because these structures have little or no prestresses.

The degradation in strength of defected structures as compared to LEFM prediction was also observed in graphene, which exhibits some nonlinear elasticity [9,11]. By contrast, a study on the fracture toughness of CNTs did not reveal such degradation, nor nonlinearity [10]. Both examples are in line with the discussion above, each from a different outlook. A study on multilayer MXene investigated its fracture toughness without comparing to LEFM, but showed that in a thicker MXene (Ti_3C_2) atoms rearrangement at the crack tip leads to layer thinning and larger dissipated energy [2]. At any rate, we expect that nonlinearity and quantization should generally apply to monolayer and multilayer MXenes of various types, as both physical mechanisms are not specific to the Ti_2C MXene described in this study, but are rather of universal nature.

4. Conclusion

MXene is a newly introduced inorganic, two-dimensional, nanoscale material with promising mechanical properties. Its processing by strong etching solutions induces defects which degrade its toughness. In this study, we investigated the fracture behavior of Ti_2C MXene by means of molecular dynamics and fracture mechanics theory. Of particular interest was finding whether MXene, a naturally brittle material, conforms to classic linear elastic fracture mechanics (LEFM), and at what scale (if any) does it resemble a continuum solid. To that end, we induced slit vacancy defects into the MXene monolayer, ranging from single-atom to 128-atom vacancies, and applied tension at a constant strain rate. By monitoring the local stress concentration at the defect tips, we were able to record the failure stress and determine the model strength and its dependence on the defect length.

We found that when the defects were very long (above ~20Å), and consequently the strength was low, the MXene strength conformed to LEFM, with fracture toughness in the order of 1.7 $MPa{\cdot}m^{0.5}$, similar to ceramic but slightly lower than graphene and SWCNT. However, in the presence of short defects of length below ~20Å, we observed a significant deviation from LEFM, amounting to as high as 30 % degradation in strength. Our theoretical analysis shows that the combination of two very different physical mechanisms is the cause for this degradation – nonlinear elasticity and energy quantization.

The first mechanism derives from the nonlinear elasticity of the MXene, witnessed by its curved stress-strain trendline. This mechanism is absent from linear atomic-scale materials such as SWCNT, which was shown to conform to LEFM [10]. The second mechanism, described by the theory of quantized fracture mechanics (QFM), accounts for the discrete steps in defect size as atoms are removed from the structure. Typically, elastic nonlinearity is difficult to model, but simplification and approximation allowed us to arrive at a closed solution for the strength. Both mechanisms manifest themselves as constant length terms added to the defect length – the nonlinearity term and the fracture quantum – the predominant one in this specific MXene structure being the former. These constant length terms ensure that the strength prediction does not diverge when the defect length tends to zero, a key discrepancy in LEFM, enabling finite strength prediction of a defect-free structure.

This study contributes to a fundamental understanding of MXene fracture toughness, as well as offering general insights for materials of similar nature. Further research is anticipated in investigating parametric variations, such as various defect shapes and orientations, loading configurations, dynamic response at high strain rates, and wide temperature range. The proposed approach may be applied in other atomic structures which exhibit similar toughness deviation and nonlinear elasticity, such as graphene and multilayer MXene. At larger size scales, the simplified nonlinearity fracture model (NLFM) may be used to explain the fracture behavior of nonlinear elastic, brittle materials, such as amorphous silica. Nanocomposite structures may be treated similarly, for example the multi-layered, laminate-like conformation of stacked MXene [42].

Funding

IG and HDW would like to acknowledge support from the G.M.J. Schmidt Minerva Centre of Supramolecular Architectures at the Weizmann Institute, and the generosity of the Harold Perlman family. LY and SJ acknowledge the financial support from the Science Foundation of the National Key Laboratory of Science and Technology on Advanced Composites in Special Environments, Harbin Institute of Technology.

Data and materials availability

All data needed to evaluate the conclusions in the paper are present in the paper and the Supplementary Materials. Additional data related to this paper may be requested from the authors.

CRediT authorship contribution statement

Israel Greenfeld: Writing – review & editing, Writing – original draft, Visualization, Validation, Project administration, Methodology, Investigation, Formal analysis, Conceptualization. **Shenda Jiang:** Writing – review & editing, Writing – original draft, Visualization, Validation, Methodology, Investigation, Formal analysis, Data curation. **Lin Yang:** Writing – review & editing, Validation, Supervision, Resources, Project administration, Funding acquisition. **H. Daniel Wagner:** Writing – review & editing, Validation, Supervision, Resources, Project administration, Funding acquisition.

Declaration of competing interest

Acknowledgements

Thanks are due to our former colleague Dr Sabyasachi Ghosh for the initiative to launch this project. SJ and LY would like to thank Dr Ma Xiaoliang and Zhang Hongchi for their help with the simulations. Additionally, we thank Dr Ali Rajabpour of Sharif University of Technology, Dr Stefan J. Eder of TU Wien, Dr Yan Xin of BeiHang University, and Dr Liu Ning of Tongji University for providing the reference materials.

Supplementary materials

Supplementary material associated with this article can be found, in the online version, at doi:10.1016/j.actamat.2025.120727.

References

[1] R.M. Ronchi, J.T. Arantes, S.F. Santos, Synthesis, structure, properties and applications of MXenes: current status and perspectives, Ceram. Int. 45 (15) (2019) 18167–18188.

[2] C. Wei, C. Wu, Nonlinear fracture of two-dimensional transition metal carbides (MXenes), Eng. Fract. Mech. 230 (2020).

[3] C.E. Shuck, M. Han, K. Maleski, K. Hantanasirisakul, S.J. Kim, J. Choi, W.E.B. Reil, Y. Gogotsi, Effect of Ti3AlC2 MAX phase on structure and properties of resultant Ti3C2Tx MXene, ACS Appl. Nano Mater. 2 (6) (2019) 3368–3376.

[4] T. Hu, J. Yang, X. Wang, Carbon vacancies in Ti(2)CT(2) MXenes: defects or a new opportunity? Phys. Chem. Chem. Phys. 19 (47) (2017) 31773–31780.

[5] Z. Guo, J. Zhou, C. Si, Z. Sun, Flexible two-dimensional Tin+1Cn (n = 1, 2 and 3) and their functionalized MXenes predicted by density functional theories, Phys. Chem. Chem. Phys. 17 (23) (2015) 15348–15354.

[6] R. Lotfi, M. Naguib, D.E. Yilmaz, J. Nanda, A.C.T. van Duin, A comparative study on the oxidation of two-dimensional Ti3C2MXene structures in different environments, J. Mater. Chem. A 6 (26) (2018) 12733–12743.

[7] H. Yu, K. Xu, Z. Zhang, X. Cao, J. Weng, J. Wu, Oxygen functionalization-induced crossover in the tensile properties of the thinnest 2D Ti2C MXene, J. Mater. Chem. C 9 (7) (2021) 2416–2425.

[8] Q. Yang, S.J. Eder, A. Martini, P.G. Grützmacher, Effect of surface termination on the balance between friction and failure of Ti3C2Tx MXenes, npj Mate. Degradation 7 (1) (2023).

[9] H. Yin, H.J. Qi, F. Fan, T. Zhu, B. Wang, Y. Wei, Griffith criterion for brittle fracture in graphene, Nano Lett. 15 (3) (2015) 1918–1924.

[10] L. Yang, I. Greenfeld, H.D. Wagner, Toughness of carbon nanotubes conforms to classic fracture mechanics, Sci. Adv. 2 (2) (2016) 1–8.

[11] M.A.N. Dewapriya, S.A. Meguid, Atomistic simulations of nanoscale crack-vacancy interaction in graphene, Carbon 125 (2017) 113–131.

[12] M.A.N. Dewapriya, R.K.N.D. Rajapakse, Atomistic and continuum modelling of stress field at an inhomogeneity in graphene, Mater Design 160 (2018) 718–730.

[13] M.A.N. Dewapriya, R.K.N.D. Rajapakse, W.P.S. Dias, Characterizing fracture stress of defective graphene samples using shallow and deep artificial neural networks, Carbon 163 (2020) 425–440.

[14] T. Shimada, K. Ouchi, Y. Chihara, T. Kitamura, Breakdown of Continuum Fracture Mechanics at the Nanoscale, Sci. Rep. 5 (2015).

[15] T. Shimada, K. Huang, L.V. Lich, N. Ozaki, B. Jang, T. Kitamura, Beyond conventional nonlinear fracture mechanics in graphene nanoribbons, Nanoscale 12 (35) (2020) 18363–18370.

[16] M.S.R. Elapolu, A. Tabarraei, X.N. Wang, D.E. Spearot, Fracture mechanics of multi-layer molybdenum disulfide, Eng. Fract. Mech. 212 (2019) 1–12.

[17] Q. Peng, Z.Y. Huang, G. Chen, Y.Q. Zhang, X.F. Zhang, X.J. Chen, Z.W. Hu, Effect of strain rate, temperature, vacancy, and microcracks on mechanical properties of 8-16-4 Graphyne, Nanomaterials-Basel 14 (6) (2024).

[18] S.M. Hatam-Lee, A. Esfandiar, A. Rajabpour, Mechanical behaviors of titanium nitride and carbide MXenes: a molecular dynamics study, Appl. Surf. Sci. 566 (2021).

[19] Y. Chen, S. Tang, X. Yan, Manipulating the crack path through the surface functional groups of MXenes, Nanoscale 14 (38) (2022) 14169–14177.

[20] M.M. Hassan, J. Islam, W.R. Sajal, M.A.-A.B. Shuvo, S. Goni, Temperature, strain rate, and point vacancy dependent anisotropic mechanical behaviors of titanium carbide (Ti3C2) MXene: a molecular dynamics study, Mater. Today Communic. 37 (2023).

[21] M.A.N. Dewapriya, Modeling Fracture of Graphene: a Molecular Dynamics Tutorial, Society of structural engineers, Sri Lanka 32 (02) (2022) 10–12.

[22] T.L. Anderson, Fracture Mechanics Fundamentals and Applications, 4 ed., CRC Press, 2017.

[23] N.M. Pugno, R.S. Ruoff, Quantized fracture mechanics, Philos. Mag. 84 (27) (2004) 2829–2845.

[24] F. Cleri, S.R. Phillpot, D. Wolf, S. Yip, Atomistic simulations of materials fracture and the link between atomic and continuum length scales, J. Am. Ceram. Soc. 81 (3) (1998) 501–516.

[25] D.P. Rooke, D.J. Cartwright, Compendium of stress intensity factors, HMSO Ministry of Defence, Procurement Executive (1976).

[26] Y. Wei, P. Zhang, R.A. Soomro, Q. Zhu, B. Xu, Advances in the synthesis of 2D MXenes, Adv. Mater. 33 (39) (2021) 2103148.

[27] Y. Tang, C. Yang, X. Xu, Y. Kang, J. Henzie, W. Que, Y. Yamauchi, MXene nanoarchitectonics: defect-engineered 2D MXenes towards enhanced electrochemical water splitting, Adv. Energy Mater. 12 (12) (2022) 2103867.

[28] A.P. Thompson, H.M. Aktulga, R. Berger, D.S. Bolintineanu, W.M. Brown, P. S. Crozier, P.J. in't Veld, A. Kohlmeyer, S.G. Moore, T.D. Nguyen, LAMMPS-a flexible simulation tool for particle-based materials modeling at the atomic, meso, and continuum scales, Comput. Phys. Commun. 271 (2022) 108171.

[29] N.C. Osti, M. Naguib, A. Ostadhossein, Y. Xie, P.R. Kent, B. Dyatkin, G. Rother, W. T. Heller, A.C. Van Duin, Y. Gogotsi, Effect of metal ion intercalation on the structure of MXene and water dynamics on its internal surfaces, ACS Appl. Mater. Interfaces 8 (14) (2016) 8859–8863.

[30] G. Plummer, B. Anasori, Y. Gogotsi, G.J. Tucker, Nanoindentation of monolayer Ti C T MXenes via atomistic simulations: the role of composition and defects on strength, Comp. Mater. Sci. 157 (2019) 168–174.

[31] Y.I. Jhon, I.K. Han, J.H. Lee, Y.M. Jhon, Microscopic understanding of exceptional orientation-dependent tensile and fracture responses of two-dimensional transition-metal carbides, Appl. Surf. Sci. 585 (2022) 152557.

[32] A. Stukowski, Visualization and analysis of atomistic simulation data with OVITO–the open visualization tool, Model Simul Mater *Sc* 18 (1) (2010).

[33] L. Yang, C. Hou, X. Ma, L. Ye, L. Chang, L. Shi, X. He, Structure relaxation via long trajectories made stable, Phys. Chem. Chem. Phys. 19 (36) (2017) 24478–24484.

[34] N. Zhang, Y. Hong, S. Yazdanparast, M.A. Zaeem, Superior structural, elastic and electronic properties of 2D titanium nitride MXenes over carbide MXenes: a comprehensive first principles study, 2D Mater. 5 (4) (2018) 045004.

[35] P. Chakraborty, T. Das, D. Nafday, L. Boeri, T. Saha-Dasgupta, Manipulating the mechanical properties of Ti2C MXene: effect of substitutional doping, Phys. Rev. B 95 (18) (2017).

[36] s. W. Ramberg, R. William, Description of stress-strain curves by three parameters, National Advisory Committee for Aeronatics, Washington, 1943, pp. 1–32.

[37] C.E. Inglis, Stresses in a plate due to the presence of cracks and sharp corners, Trans. Inst. Naval Archit. 55 (1913) 219–241.

[38] W.d. Pilkey, Peterson's Stress Concentration Factors, 2nd ed., John Wiley & Sons, Inc, 1997.

[39] A.A. Griffith, Phenomena of Rupture and Flow in Solids, Philos Tr R Soc S-A 221 (1921) 163–198.

[40] T. Hao, Z.M. Hossain, Atomistic mechanisms of crack nucleation and propagation in amorphous silica, Phys. Rev. B 100 (1) (2019).

[41] M.F. Ashby, Materials Selection in Mechanical Design, Elsevier, Burlington, MA, USA, 2011. Fourth Edition ed.

[42] Y. Li, C. Wei, S. Huang, A. Ghasemi, W. Gao, C. Wu, V.N. Mochalin, Situ tensile testing of nanometer-thick two-dimensional transition-metal carbide films: implications for mxenes acting as nanoscale reinforcement agents, ACS Appl. Nano Mater. 4 (5) (2021) 5058–5067.